Fast Crystallization Driven by Quasiatomic Electrons at Ultralow Temperatures

Long Zhao,[1] Hongxiang Zong,[1,*] Artem R. Oganov,[2] Xiangdong Ding,[1,†] Jun Sun,[1] and Graeme J. Ackland[3]
[1]State Key Laboratory for Mechanical Behavior of Materials, Xi'an Jiaotong University, Xi'an 710049, China
[2]Skolkovo Institute of Science and Technology, Skolkovo Innovation Center, Bolshoy Boulevard 30, Building 1, Moscow 121205, Russia
[3]Centre for Science at Extreme Conditions (CSEC), School of Physics and Astronomy, University of Edinburgh, Edinburgh EH9 3FD, United Kingdom

(Received 18 March 2025; revised 25 June 2025; accepted 22 August 2025; published 10 September 2025)

In electride liquids, electrons detach from atomic orbitals and freely occupy the interstitial regions, forming quasiatomic electrons. Here, using dense electride potassium liquid as an example, we uncover a fast crystallization behavior at ultralow temperatures. By combining machine-learned molecular dynamic simulations and *ab initio* calculations, we demonstrate that this rapid crystallization is attributed to quasiatomic electron flexibility, i.e., self-accommodation of atom size with the help of the change of quasiatomic electrons, particularly the population of involved quasiatomic electrons that is enhanced at low temperatures. This effect not only accelerates atomic mobility but also softens the stiffness of the solid-liquid interface, triggering supercollective atomic motion and enabling rapid crystallization. Our findings challenge conventional views of crystallization kinetics and reveal a previously unrecognized mechanism where electronic contributions play a dominant role in dictating metallic solidification.

DOI: 10.1103/lp46-x2wy

Crystallization from deeply supercooled liquids is a fundamental process in condensed matter physics and materials science [1–6], playing a pivotal role in both natural phenomena and technological applications [1,7,8]. Classical theories of crystallization tell us that the crystal growth rate is expressed as $K(T)[1-\exp(-\Delta\mu/k_BT)]$, where $K(T)$ is the kinetic factor expressing the rate of atom addition to the crystal, T is the temperature, k_B is the Boltzmann constant, and Δu is the difference in crystal and liquid chemical potentials [9]. In deeply supercooled liquids, crystallization kinetics are predominantly governed by $K(T)$, which is constrained by diffusion and structural frustration [10–12]. As the temperature decreases, reduced particle mobility and geometric frustration sharply suppress crystal growth, potentially leading to vitrification at ultralow temperatures [13,14]. This behavior has been widely observed in experiments and simulations across various supercooled liquids [15–18].

High-pressure electride (HPE) liquids represent an extraordinary class of matter where electrons detach from parent atoms and localize in the interstitial voids of disordered atomic structures, forming so-called quasiatomic electrons [19–23]. The existence of quasiatomic electrons in liquids was first predicted in dense potassium [24] and later experimentally verified in shock-compressed sodium [25]. Recent studies have demonstrated that the quasiatomic electrons fundamentally reshape phase dynamics, challenging conventional paradigms in condensed matter physics [24,26–30]. For instance, HPE liquids exhibit anomalous dynamical behavior, such as pressure-independent diffusivity plateaus and anharmonicity-induced one-dimensional (1D) atomic motion [24,27,29], as well as a marked enhancement in the Debye-Waller factor even at ~50 K, highlighting the interplay between electron localization and atomic motion [28]. These findings inspired us to raise the question of whether the quasiatomic electrons can challenge the traditional crystallization kinetics, enabling fast crystallization at ultralow temperatures. Beyond their intrinsic scientific interest, HPE liquids likely exist in planetary interiors [31], as many high-pressure materials—including alkali metals [32,33], alkaline earth metals [29,34], magnesium [35], carbon [36], and compounds like Mg_3O_2 [37], Na_3Cl [38], and SiO [39]—exhibit electride characteristics in their crystalline phases. Understanding the crystallization kinetics of HPE liquids is, therefore, not only critical for advancing our knowledge of condensed matter physics but also for interpreting planetary formation and evolution under extreme environments.

Here, we take dense potassium as an example to investigate the crystallization kinetics of electride liquid through molecular dynamics (MD) simulations, powered by a temperature-dependent machine learning potential (TD-MLP). This potential explicitly incorporates the electron-smearing effects into the total energy calculation, providing a reliable description of electride systems across a wide temperature range (see Notes 1–2 in [40] for details

*Contact author: zonghust@mail.xjtu.edu.cn
†Contact author: dingxd@mail.xjtu.edu.cn

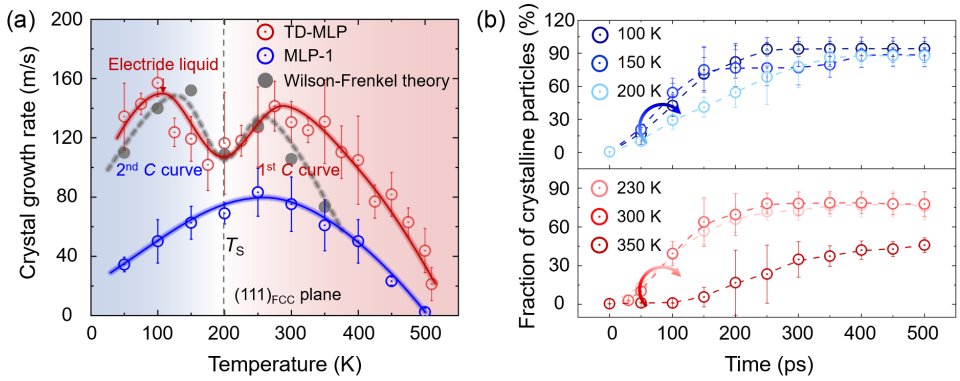

FIG. 1. Crystallization kinetics of dense electride liquid in potassium. (a) Temperature dependence of the average crystal growth rate for $(111)_{FCC}$ plane. Red circles represent results from the TD-MLP model, showing a double-C curve phenomenon separated by a characteristic temperature ($T_s = 200$ K). In contrast, another MLP model (referred to as MLP-1) was trained without explicit electronic contributions to the total energy. Its results exhibit a single C curve (blue circles). Gray circles correspond to crystal growth rates predicted by the modified Wilson-Frenkel theory. (b) Time evolution of the fraction of crystalline particles for electride liquid at different temperatures. The lower and upper panels illustrate the evolution of crystalline fractions above and below 200 K, respectively. Each data point is averaged over ten independent simulations, with error bars denoting the standard deviation.

and validation). Surprisingly, we observe an unprecedented enhancement in the crystal growth rate at ultralow temperatures ($\sim 0.2T_m$), defying the expected sluggish dynamics and the occurrence of icosahedron frustration in such deeply supercooled states [8,10,15]. It is believed that vitrification will be triggered when quenching liquid down to $\sim 0.385T_m$ (i.e., the theoretical lower boundary of glass transition temperatures for metallic systems [66–68]) with an ultrafast cooling rate.

We first investigated the crystal growth behavior of potassium at 15 GPa across temperatures (see Note 3 in [40] for computational details). The growth rate was determined by tracking the propagation of the $(111)_{FCC}$ plane in a solid-liquid interface model [Fig. S5], and averaged over ten independent simulations, as shown by the red circles in Fig. 1(a). The temperature dependence of the growth rate exhibits a distinctive profile characterized by double-C curves, separated by approximately 200 K. The first C curve ($T > 200$ K) features a nearly linear increase in growth rate followed by a turnover and subsequent decrease as the temperature is reduced, consistent with crystallization kinetics observed in metals and simple colloidal systems [15–18]. Remarkably, a second C curve emerges below 200 K, indicating a re-acceleration of the crystal growth rate. This secondary acceleration culminates in a maximum growth rate of approximately 150 m/s at 100 K. Below this temperature, the growth rate begins to decline, yet it remains remarkably high, exceeding 120 m/s at temperatures as low as 50 K ($\sim 0.1\ T_m$, $T_m = 515 \pm 10$ K). These results provide compelling evidence for fast crystallization in electride liquids, even in deeply supercooled states. Moreover, this double-C curve phenomenon appears to be independent of the crystalline surface orientation, as similar fast crystallization behavior was observed for other crystalline-liquid interface models, including the $(110)_{FCC}$ and $(112)_{FCC}$ planes (Fig. S7).

We further examined the crystallization kinetics of potassium from a completely supercooled liquid at 15 GPa. Below T_m, the FCC structure is the thermodynamically stable phase [54]. Crystalline particles were identified using bond-orientational order parameters (i.e., $q_6 > 0.43$ for FCC) [15]. Figure 1(b) depicts the evolution of the fraction of crystalline particles at various temperatures from 50 to 400 K. As anticipated, the crystallization rate shows a nonmonotonic temperature dependence, evident in the time-dependent mole fraction of crystalline particles. The FCC nucleation behavior can be classified into two categories based on temperature. Above 200 K, crystallization involves a detectable incubation stage followed by rapid growth and eventual saturation [the upper panel of Fig. 1(b)]. In contrast, below 200 K, crystallization occurs rapidly without an observable incubation stage, and the mole fraction of FCC particles grows rapidly and then tends to saturation [the lower panel of Fig. 1(b)]. The corresponding representative atomic structural evolutions are depicted in Fig. S8. The supercooled electride liquid can crystallize into either a single crystal or a polycrystal due to the competition between nucleation and growth processes [69]. More importantly, the slopes of the time-dependent crystalline particle fraction first increase and then decrease, with an inflection point at 150 K. This behavior is consistent with the secondary C-curve phenomenon observed in Figs. 1(a) and S7, providing further evidence for fast crystallization at ultralow temperatures in electride liquids.

Figure 2(a) shows the temperature-dependent atomic mean square displacements (MSDs) throughout the crystallization process. All MSD profiles exhibit two distinct regimes: an initial linear increase followed by a long

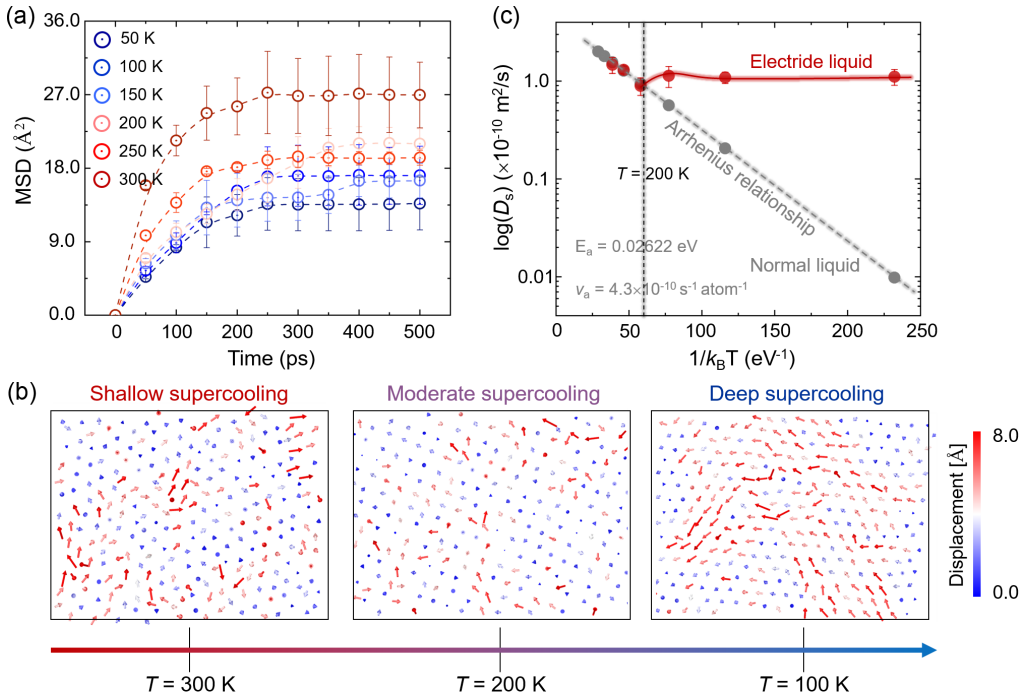

FIG. 2. Diffusive behavior of dense electride liquid during crystallization. (a) Time evolution of the mean square displacements (MSDs) at different temperatures, corresponding to crystalline particle fractions varying from ~5.0% to ~90.0%. (b) The temperature-dependent short-time diffusion coefficients (D_s). Red circles represent the TD-MLP results, while gray circles represent data derived from the Arrhenius relationship. The activation energy ($E_a = 0.02622$ eV) and attempt frequency ($V_a = 4.3 \times 10^{-10}\,s^{-1}\,atom^{-1}$) are obtained by fitting diffusion coefficients above 200 K. Solid and dashed lines are guides to the eye of these data. (c) Two-dimensional particle displacement field of particles within a single crystal plane postcrystallization at shallow ($T = 300$ K), moderate ($T = 200$ K), and deep supercooling ($T = 100$ K). Arrows show the particle displacement vectors, while color variations represent their magnitudes, with blue and red indicating small and large displacement, respectively.

plateau. The emergence of the plateau signifies the completion of crystallization, as atomic motion transitions to localized vibrations within the crystal lattice. Interestingly, a striking abnormality emerges when the electride liquid is quenched below 200 K: the MSDs exhibit a negative temperature dependence. In stark contrast to normal liquids, where MSDs remain below 1.0 Å^2, the deeply supercooled electride liquid in potassium exhibits significantly larger MSDs, exceeding 10.0 Å^2, indicating anomalous atomic motion beyond typical subdiffusive processes [70].

A detailed examination of the corresponding displacement fields reveals the presence of supercollective motion in the deeply supercooled electride liquid. This phenomenon is characterized by a high proportion of particles engaging in collective motion with large displacements. As illustrated in Fig. 2(b), we compare the two-dimensional (2D) displacement fields of particles within a single-layer crystal postcrystallization at three representative temperatures, corresponding to shallow, moderate, and deep supercooling. At 300 K (shallow supercooling), the displacement vectors are large but random, indicative of random atomic motion [right panel in Fig. 2(b)]. As the temperature decreases to 200 K (moderate supercooling), the magnitude of displacement vectors diminishes, reflecting a reduction in particle mobility [middle panel in Fig. 2(b)]. However, under deep supercooling at 100 K, atomic motion becomes highly coordinated, with ~5.0 Å displacements aligning across many particles, highlighting the emergence of supercollective motion [left panel in Fig. 2(b)].

To further elucidate the dynamics, we extracted the temperature-dependent diffusion coefficients (D) from the linear regime of the MSD profiles [Fig. 2(c)]. These short-time D_s values capture the high nonequilibrium early stage of crystallization and are distinct from long-time, equilibrium diffusion coefficients [15]. The temperature dependence of D_s reveals two distinct regimes. Above 200 K, D_s follows Arrhenius' law, indicating thermally activated diffusive motion. Below 200 K, however, D_s becomes nearly temperature-independent, reflecting a fundamentally different diffusive mechanism. While non-Arrhenius temperature-dependent diffusivity is commonly observed in supercooled metallic liquids and typically described by the Volmer-Fulcher-Tammann formula [71], the observed behavior in deeply supercooled electride liquids differs markedly. Our discussion below attributes this deviation to the interplay between quasiatomic electrons and atomic motion in electride liquids that governs

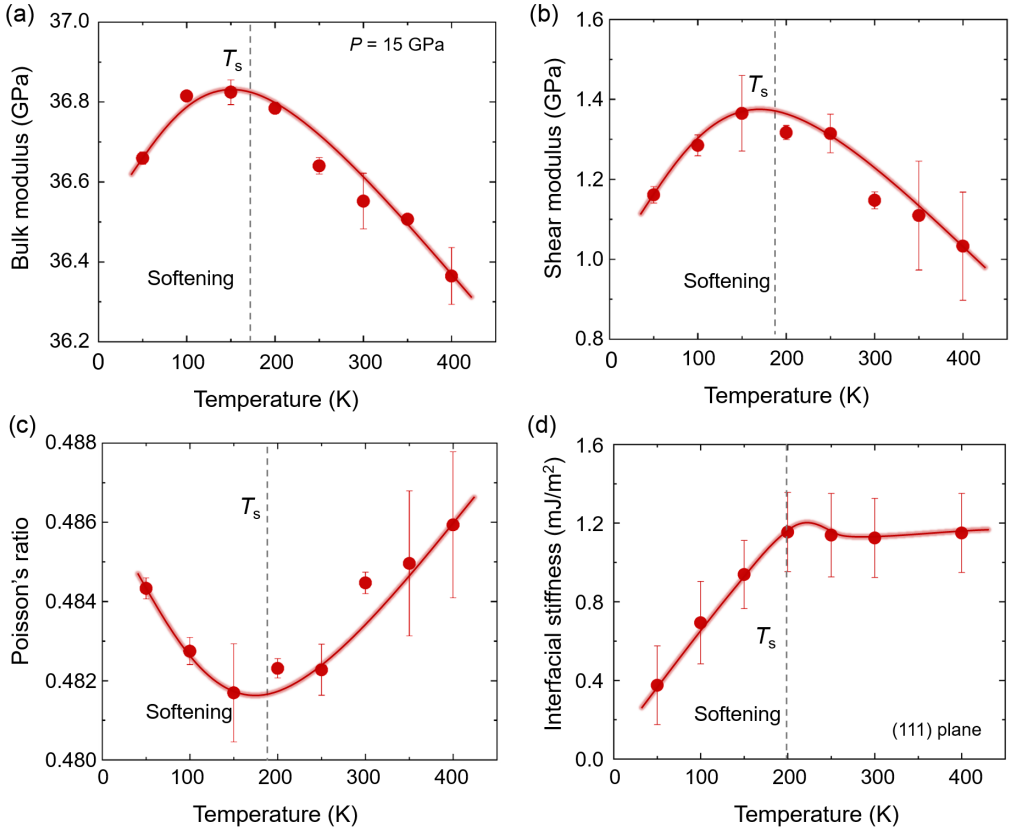

FIG. 3. Temperature-dependent thermodynamics of dense electride potassium. (a)–(c) Temperature dependence of bulk modulus, shear modulus, and Poisson's ratio of the FCC crystal phase at 15 GPa, respectively. (d) Temperature-dependent interfacial stiffness of $(111)_{\mathrm{FCC}}$-supercooled liquid interface. Dashed line indicates the crossover temperature of the thermodynamic properties. Solid lines are guides to the eye.

the observed supercollective dynamics, enabling fast, temperature-independent diffusion in the deeply supercooled regime.

Figures 3(a) and 3(b) illustrate the temperature dependence of the bulk and shear moduli of the FCC crystal phase. From a thermodynamic perspective, the energy barrier for crystal nucleation arises from interfacial energy and elastic mismatch penalties, both governed by the crystal's elastic modulus [72]. As expected, these moduli generally increase with decreasing temperature due to suppressed atomic motion. However, an anomalous softening is observed below ~200 K. This is further supported by a Poisson's ratio increase to ~0.5 at low temperatures [Fig. 3(c)], comparable to that of soft materials like rubber [73]. We propose that this low-temperature softening of the bulk and shear moduli contributes to reducing both the surface tension and the misfit strain energy at the supercooled liquid-solid boundary, thereby reducing the nucleation barrier of crystal nucleus. This hypothesis is supported by a marked decrease in interfacial stiffness below ~200 K [Figs. 3(d) and S9], obtained using the capillary fluctuation method [64] (see Note 4 in [40]). This contrasts with the prevailing expectation that interfacial stiffness increases as temperature decreases [74].

A modified Wilson-Frenkel model [17] incorporating temperature-dependent interfacial stiffness is employed to describe the double-C crystallization kinetics of electride liquids. The growth rate is given by

$$V(T) = \frac{6\ell}{\lambda^2} D \left[1 - \exp\left(-\frac{\Delta\mu(T)}{k_B T}\right)\right] S(T), \qquad (1)$$

where ℓ and λ are, respectively, the interplanar spacing and the displacement length. $S(T)$ accounts for the temperature dependence of interfacial energy. The modified Wilson-Frenkel model accurately predicted the crystal growth rates along different crystalline planes across a range of temperatures, which agrees well with TD-MLP simulations [Fig. 1(a) and Fig. S7]. This highlights the key roles of atomic mobility and temperature-dependent interfacial stiffness in describing the double-C curve phenomenon.

Unlike conventional metallic liquids [4], electride liquids host quasiatomic electrons in interstitial voids, providing an additional degree of freedom that may influence crystallization kinetics. To investigate this, we first analyzed the temperature dependence of electride density in supercooled potassium liquids. Figure 4(a) shows the quasiatomic electron population (n_e) at 15 GPa, estimated using

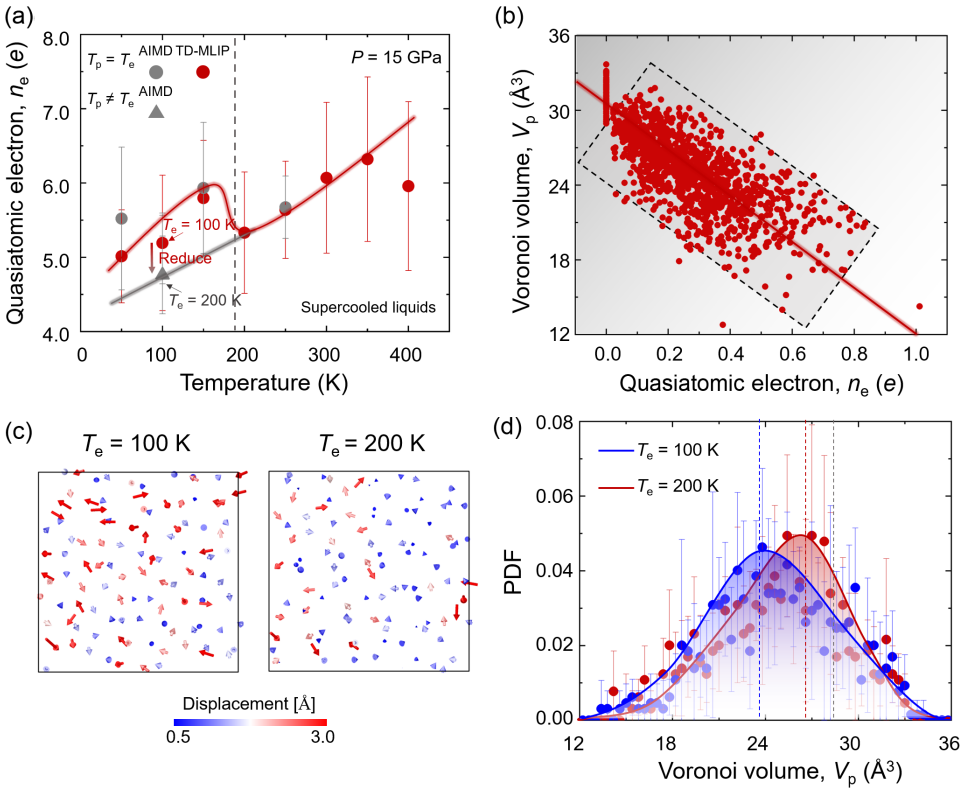

FIG. 4. Quasiatomic electron flexibility of dense electride liquid. (a) Temperature dependence of quasiatomic electron population (n_e) in supercooled electride liquid at 15 GPa. All data were obtained by performing density-functional theory calculations on snapshots extracted from TD-MLP MD and AIMD simulations, followed by Bader charge analysis. Red and gray circles represent n_e for TD-MLP MD and AIMD snapshots, respectively, under the matched electronic (T_e) and particle temperatures (T_p). The gray triangle denotes n_e for AIMD snapshots at $T_e = 200$ K and $T_p = 100$ K. Each data point is averaged over ten independent snapshots. Error bars indicate the standard deviation of n_e among the ten snapshots in each scenario. (b) Correlation between local quasiatomic electron density (n_e) and particle Voronoi volume (V_p) in the supercooled liquid. The local quasiatomic electron density is calculated within a 3.0 Å cutoff around the individual particle. (c) Two-dimensional (2D) displacement field of particles during the incubation stage of crystallization at $T_e = 100$ K and $T_e = 200$ K. Arrows show the particle displacement vectors, while color variations represent their magnitudes, with blue and red indicating small and large displacement, respectively. (d) Probability distribution function (PDF) of particle Voronoi volume in deeply supercooled electride liquids ($T_p = 100$ K) at different electronic temperatures ($T_e = 100$ K and $T_e = 200$ K). Both solid and dashed lines are guides to the eye.

Bader analysis to decompose the charge density [67]. The data were averaged over ten independent snapshots with 108 atoms extracted from MD simulations with TD-MLP before crystallization. The results reveal a two-stage temperature dependence with an abrupt increase in n_e at ~200 K. Above 200 K, the n_e remains stable at ~5.0e, while below 200 K, it rises significantly to ~6.0e before stabilizing at ~5.0e as the temperature decreases to 50 K. This trend is further corroborated by electronic structure calculations from *ab initio* molecular dynamics (AIMD) snapshots [gray circles in Fig. 4(a)]. The pronounced change of n_e at 200 K may indicate a liquid-liquid phase transition as the temperature decreases. Notably, this two-regime behavior mirrors the double-C crystallization kinetics, supporting the role of quasiatomic electrons in influencing crystallization.

To further understand the influence of quasiatomic electrons, we examined the correlation between local n_e and atomic volume (V_p) using a $n_e - V_p$ plot [Fig. 4(b)]. A negative correlation was observed: the V_p decreases as the n_e increases. This suggests that quasiatomic electrons provide flexibility to adjust the local particle size, enabling atoms to better accommodate their surrounding environment—a property we refer to as quasiatomic electron flexibility. Such electronic flexibility was previously linked to fast mass transport and elastic softness during the transition from free-electron to electride liquids [24]. This property enhances the adaptability of particles, facilitating crystallization even in deeply supercooled states.

To directly connect quasiatomic electron flexibility to crystallization kinetics, we modulated the n_e at a fixed atomic temperature (T_p) by adjusting the electronic temperature (T_e) using the Fermi smearing method. This approach reduces the n_e as T_e increases while maintaining constant T_p during AIMD simulations [Fig. S10]. Figure 4(c) illustrates the 2D displacement field of particles during

the incubation stage of crystallization at different T_e. As T_e increases from 100 to 200 K, particle mobility decreases sharply, as evidenced by reduced displacement magnitudes. This observation is further supported by the probability distribution functions of atomic displacements [Fig. S11]. Importantly, the atomic configurations of both liquids ($T_e = 100$ and $T_e = 200$ K) show no resolvable differences [Fig. S12], suggesting that quasiatomic electrons, rather than structural frustration, govern the crystallization behavior. The associated increase in particle size with decreasing quasiatomic electrons [gray triangle in Figs. 4(a) and 4(d)] further confirms the role of quasiatomic electron flexibility in crystallization.

Before concluding, we conducted additional MD simulations of the $(111)_{FCC}$ liquid-crystal model using two other MLPs: MLP-1 (excluding explicit electronic contributions) and MLP-2 (trained on potential energy only). Both yield nearly single *C*-shaped growth curves [blue circles Figs. 1(a) and S13], in contrast to the double-*C* curve observed with TD-MLP, and predict significantly lower growth rates across all temperatures. These results underscore the pivotal role of quasiatomic electron flexibility in driving fast crystallization from deeply supercooled electride liquids. Notably, it promotes both nucleation and growth, with a more pronounced effect on the latter [Fig. S14]. In summary, we reveal an unexpectedly fast crystallization process in electride liquids of potassium at ultralow temperatures, a stark contrast to the inhibited crystallization typically observed in deeply supercooled liquids due to sluggish dynamics and geometric frustrations [10,11,13]. We believe that such rapid crystallization kinetics is a general phenomenon for electride liquids, as evidenced by similar behavior in high-pressure calcium [Fig. S15]. This phenomenon is attributed to the unique flexibility of quasiatomic electrons, which reversibly switch between free-electron and electride states, enhancing both particle mobility and elastic stiffness. This mechanism differs fundamentally from barrierless collective crystallization observed in charged colloidal systems, where ultrafast crystallization is driven by wall confinement at low temperatures [70]. Direct experimental validation may be achieved using a temperature-controlled diamond anvil cell combined with x-ray free-electron laser techniques [25,75,76]. More importantly, some electrides, such as $[Ca_2N]^+e^-$ and $[RE_2C]^{2+}2e^-$ (with RE = Y, Sc, and Gd) [77–81], can exist under ambient conditions, offering an additional platform for experimental validation.

The discovery of fast crystallization in electride liquids may have profound implications for planetary science. Electride-enriched planetary interiors, such as those of giant planets, likely host rapid crystallization processes that could significantly alter thermal and compositional evolution. Furthermore, our findings highlight the necessity of incorporating electronic degrees of freedom into machine learning potentials for accurate modeling of high-pressure materials, providing a framework to explore the interplay between electronic structure and macroscopic phenomena in complex systems.

Acknowledgments—This work was supported by the National Natural Science Foundation of China (52322103 and 12304026), the China Postdoctoral Science Foundation (2023M742806), and the 111 projects 2.0 (BP2018008).

X. D., H. Z., and L. Z. supervised the project. L. Z. conceived the idea, designed, and performed the simulations. L. Z., H. Z., A. R. O., X. D., and G. J. A. discussed and analyzed the data and wrote the manuscript. J. S. participated in data interpretation and manuscript correction. All authors contributed to commenting on the manuscript and discussing the results.

The authors declare that they have no competing financial interests.

Data availability—The data that support the findings of this Letter are openly available [82].

[1] J. Christian, *The Theory of Transformations in Metals and Alloys* (Pergamon, Oxford, 2002).
[2] L. Gránásy, T. Pusztai, T. Börzsönyi, J. A. Warren, and J. F. Douglas, A general mechanism of polycrystalline growth, Nat. Mater. **3**, 645 (2004).
[3] L. Gránásy, T. Pusztai, J. A. Warren, J. F. Douglas, T. Börzsönyi, and V. Ferreiro, Growth of 'dizzy dendrites' in a random field of foreign particles, Nat. Mater. **2**, 92 (2003).
[4] H. Tanaka, H. Tong, R. Shi, and J. Russo, Revealing key structural features hidden in liquids and glasses, Nat. Rev. Phys. **1**, 333 (2019).
[5] W. Zhang, R. Mazzarello, M. Wuttig, and E. Ma, Designing crystallization in phase-change materials for universal memory and neuro-inspired computing, Nat. Rev. Mater. **4**, 150 (2019).
[6] T. Sato, K. Miyagawa, and K. Kanoda, Electronic crystal growth, Science **357**, 1378 (2017).
[7] J. Kim, Y. Kimura, B. Puchala, T. Yamazaki, U. Becker, and W. Sun, Dissolution enables dolomite crystal growth near ambient conditions, Science **382**, 915 (2023).
[8] J. Russo, F. Romano, and H. Tanaka, Glass forming ability in systems with competing orderings, Phys. Rev. X **8**, 021040 (2018).
[9] K. Kelton and A. L. Greer, *Nucleation in Condensed Matter: Applications in Materials and Biology* (Elsevier, New York, 2010).
[10] J. Orava and A. L. Greer, Fast and slow crystal growth kinetics in glass-forming melts, J. Chem. Phys. **140**, 214504 (2014).
[11] P. G. Debenedetti and F. H. Stillinger, Supercooled liquids and the glass transition, Nature (London) **410**, 259 (2001).

[12] N. Francois, M. Saadatfar, R. Cruikshank, and A. Sheppard, Geometrical frustration in amorphous and partially crystallized packings of spheres, Phys. Rev. Lett. **111**, 148001 (2013).
[13] H. Shintani and H. Tanaka, Frustration on the way to crystallization in glass, Nat. Phys. **2**, 200 (2006).
[14] L. Berthier, P. Charbonneau, D. Coslovich, A. Ninarello, M. Ozawa, and S. Yaida, Configurational entropy measurements in extremely supercooled liquids that break the glass ceiling, Proc. Natl. Acad. Sci. U.S.A. **114**, 11356 (2017).
[15] M. Zhan, Y. Chen, Z. Jiang, N. Xu, and P. Tan, Multiple scenarios of low-temperature nucleation in simple liquids, Phys. Rev. Lett. **130**, 178201 (2023).
[16] G. Sun, J. Xu, and P. Harrowell, The mechanism of the ultrafast crystal growth of pure metals from their melts, Nat. Mater. **17**, 881 (2018).
[17] Y.-C. Hu and H. Tanaka, Revealing the role of liquid preordering in crystallisation of supercooled liquids, Nat. Commun. **13**, 4519 (2022).
[18] Y. Ashkenazy and R. S. Averback, Kinetic stages in the crystallization of deeply undercooled body-centered-cubic and face-centered-cubic metals, Acta Mater. **58**, 524 (2010).
[19] M.-S. Miao and R. Hoffmann, High pressure electrides: A predictive chemical and physical theory, Acc. Chem. Res. **47**, 1311 (2014).
[20] X. Dong and A. R. Oganov, in *Correlations in Condensed Matter Under Extreme Conditions: A Tribute to Renato Pucci on the Occasion of his 70th Birthday*, edited by G. G. N. Angilella and A. La Magna (Springer International Publishing, Cham, 2017).
[21] M. Miao, Y. Sun, E. Zurek, and H. Lin, Chemistry under high pressure, Nat. Rev. Chem. **4**, 508 (2020).
[22] H. Hosono and M. Kitano, Advances in materials and applications of inorganic electrides, Chem. Rev. **121**, 3121 (2021).
[23] S. Racioppi and E. Zurek, High-pressure electrides: A quantum chemical perspective, Annu. Rev. Mater. Res. **55**, 1 (2025).
[24] H. Zong, V. N. Robinson, A. Hermann, L. Zhao, S. Scandolo, X. Ding, and G. J. Ackland, Free electron to electride transition in dense liquid potassium, Nat. Phys. **17**, 955 (2021).
[25] D. N. Polsin *et al.*, Structural complexity in ramp-compressed sodium to 480 GPa, Nat. Commun. **13**, 2534 (2022).
[26] L. Zhang, H. Y. Geng, and Q. Wu, Prediction of anomalous LA-TA splitting in electrides, Matter Radiat. Extremes **6**, 038403 (2021).
[27] S. Ayrinhac, V. N. Robinson, F. Decremps, M. Gauthier, D. Antonangeli, S. Scandolo, and M. Morand, High-pressure transformations in liquid rubidium, Phys. Rev. Mater. **4**, 113611 (2020).
[28] L. Zhao, H. Zong, X. Ding, J. Sun, and G. J. Ackland, Anomalous thermophysical properties and electride transition in fcc potassium, Phys. Rev. B **104**, 104107 (2021).
[29] Y. Wang, J. Wang, A. Hermann, C. Liu, H. Gao, E. Tosatti, H.-T. Wang, D. Xing, and J. Sun, Electronically driven 1D cooperative diffusion in a simple cubic crystal, Phys. Rev. X **11**, 011006 (2021).
[30] L. E. Johnson, P. V. Sushko, Y. Tomota, and H. Hosono, Electron anions and the glass transition temperature, Proc. Natl. Acad. Sci. U.S.A. **113**, 10007 (2016).
[31] I. Park, Y. He, H.-k. Mao, J. H. Shim, and D. Y. Kim, Electride formation of HCP-iron at high pressure: Unraveling the origin of the superionic state of iron-rich compounds in rocky planets, Adv. Sci. **11**, 2308177 (2024).
[32] C. L. Guillaume, E. Gregoryanz, O. Degtyareva, M. I. McMahon, M. Hanfland, S. Evans, M. Guthrie, S. V. Sinogeikin, and H. K. Mao, Cold melting and solid structures of dense lithium, Nat. Phys. **7**, 211 (2011).
[33] Y. Ma, M. Eremets, A. R. Oganov, Y. Xie, I. Trojan, S. Medvedev, A. O. Lyakhov, M. Valle, and V. Prakapenka, Transparent dense sodium, Nature (London) **458**, 182 (2009).
[34] A. R. Oganov, Y. Ma, Y. Xu, I. Errea, A. Bergara, and A. O. Lyakhov, Exotic behavior and crystal structures of calcium under pressure, Proc. Natl. Acad. Sci. U.S.A. **107**, 7646 (2010).
[35] M. G. Gorman *et al.*, Experimental observation of open structures in elemental magnesium at terapascal pressures, Nat. Phys. **18**, 1307 (2022).
[36] M. Martinez-Canales, C. J. Pickard, and R. J. Needs, Thermodynamically stable phases of carbon at multiterapascal pressures, Phys. Rev. Lett. **108**, 045704 (2012).
[37] Q. Zhu, A. R. Oganov, and A. O. Lyakhov, Novel stable compounds in the Mg-O system under high pressure, Phys. Chem. Chem. Phys. **15**, 7696 (2013).
[38] W. Zhang, A. R. Oganov, A. F. Goncharov, Q. Zhu, S. Eddine Boulfelfel, A. O. Lyakhov, E. Stavrou, M. Somayazulu, V. B. Prakapenka, and Z. Konôpková, Unexpected stable stoichiometries of sodium chlorides, Science **342**, 1502 (2013).
[39] H. Niu, A. R. Oganov, X.-Q. Chen, and D. Li, Prediction of novel stable compounds in the Mg-Si-O system under exoplanet pressures, Sci. Rep. **5**, 18347 (2015).
[40] See Supplemental Material at http://link.aps.org/supplemental/10.1103/lp46-x2wy for details about the description and benchmark of TD-MLP, as well as simulation details for both AIMD and TD-MLP MD simulations, which includes Refs. [41–65].
[41] A. P. Bartók, M. C. Payne, R. Kondor, and G. Csányi, Gaussian approximation potentials: The accuracy of quantum mechanics, without the electrons, Phys. Rev. Lett. **104**, 136403 (2010).
[42] H. Wang, L. Zhang, J. Han, and W. E, DeePMD-kit: A deep learning package for many-body potential energy representation and molecular dynamics, Comput. Phys. Commun. **228**, 178 (2018).
[43] G. J. Ackland, Temperature dependence in interatomic potentials and an improved potential for Ti, J. Phys. Conf. Ser. **402**, 012001 (2012).
[44] G. Kresse and J. Furthmüller, Efficient iterative schemes for *ab initio* total-energy calculations using a plane-wave basis set, Phys. Rev. B **54**, 11169 (1996).
[45] N. D. Mermin, Thermal properties of the inhomogeneous electron gas, Phys. Rev. **137**, A1441 (1965).
[46] G. J. Ackland and S. K. Reed, Two-band second moment model and an interatomic potential for caesium, Phys. Rev. B **67**, 174108 (2003).

[47] L. Zhao, H. Zong, X. Ding, J. Sun, and G. J. Ackland, Commensurate-incommensurate phase transition of dense potassium simulated by machine-learned interatomic potential, Phys. Rev. B **100**, 220101 (2019).
[48] H. Li, L. Zhao, X. Ding, H. Zong, T. Lookman, and J. Sun, Mechanism of the β to ω phase transformation in shock compressed Zr-Nb alloys, Phys. Rev. B **110**, 134105 (2024).
[49] S. Plimpton, Fast parallel algorithms for short-range molecular dynamics, J. Comput. Phys. **117**, 1 (1995).
[50] H. Zong, H. Wiebe, and G. J. Ackland, Understanding high pressure molecular hydrogen with a hierarchical machine-learned potential, Nat. Commun. **11**, 5014 (2020).
[51] Y. Wang and J. P. Perdew, Correlation hole of the spin-polarized electron gas, with exact small-wave-vector and high-density scaling, Phys. Rev. B **44**, 13298 (1991).
[52] C. J. Pickard and R. J. Needs, *Ab initio* random structure searching, J. Phys. Condens. Matter **23**, 053201 (2011).
[53] G. Woolman, V. Naden Robinson, M. Marqués, I. Loa, G. J. Ackland, and A. Hermann, Structural and electronic properties of the alkali metal incommensurate phases, Phys. Rev. Mater. **2**, 053604 (2018).
[54] E. E. McBride, K. A. Munro, G. W. Stinton, R. J. Husband, R. Briggs, H. P. Liermann, and M. I. McMahon, One-dimensional chain melting in incommensurate potassium, Phys. Rev. B **91**, 144111 (2015).
[55] E. Oren, D. Kartoon, and G. Makov, Machine learning-based modeling of high-pressure phase diagrams: Anomalous melting of Rb, J. Chem. Phys. **157**, 014502 (2022).
[56] D. Alfè, M. J. Gillan, and G. D. Price, Complementary approaches to the *ab initio* calculation of melting properties, J. Chem. Phys. **116**, 6170 (2002).
[57] D. Alfè, Melting curve of MgO from first-principles simulations, Phys. Rev. Lett. **94**, 235701 (2005).
[58] S. Nosé, A unified formulation of the constant temperature molecular dynamics methods, J. Chem. Phys. **81**, 511 (1984).
[59] M. Parrinello and A. Rahman, Polymorphic transitions in single crystals: A new molecular dynamics method, J. Appl. Phys. **52**, 7182 (1981).
[60] A. Stukowski, Visualization and analysis of atomistic simulation data with OVITO–the open visualization tool, Model. Simul. Mater. Sci. Eng. **18**, 015012 (2010).
[61] P. Tan, N. Xu, and L. Xu, Visualizing kinetic pathways of homogeneous nucleation in colloidal crystallization, Nat. Phys. **10**, 73 (2014).
[62] Y. Yin, Y. Zhu, S. Liu, D. Zheng, and M. Yi, Far-from-equilibrium solid–liquid interfacial properties of aluminum, Acta Mater. **278**, 120279 (2024).
[63] C. Qi, J. F. Li, B. Xu, L. T. Kong, and S. Zhao, Atomistic characterization of solid-liquid interfaces in the Cu-Ni binary alloy system, Comput. Mater. Sci. **125**, 72 (2016).
[64] J. Hoyt, M. Asta, and A. Karma, Method for computing the anisotropy of the solid-liquid interfacial free energy, Phys. Rev. Lett. **86**, 5530 (2001).
[65] V. Erukhimovitch and J. Baram, Nucleation and growth transformation kinetics, Phys. Rev. B **51**, 6221 (1995).
[66] Z. Lu and J. Li, Correlation between average melting temperature and glass transition temperature in metallic glasses, Appl. Phys. Lett. **94**, 061913 (2009).
[67] C. R. Cao, D. W. Ding, D. Q. Zhao, E. Axinte, H. Y. Bai, and W. H. Wang, Correlation between glass transition temperature and melting temperature in metallic glasses, Mater. Des. **60**, 576 (2014).
[68] P. Lunkenheimer, A. Loidl, B. Riechers, A. Zaccone, and K. Samwer, Thermal expansion and the glass transition, Nat. Phys. **19**, 694 (2023).
[69] U. Pinsook and G. J. Ackland, Simulation of martensitic microstructural evolution in zirconium, Phys. Rev. B **58**, 11252 (1998).
[70] Q. Gao *et al.*, Fast crystal growth at ultra-low temperatures, Nat. Mater. **20**, 1431 (2021).
[71] T. Wang, F. Zhang, L. Yang, X. W. Fang, S. H. Zhou, M. J. Kramer, C. Z. Wang, K. M. Ho, and R. E. Napolitano, A computational study of diffusion in a glass-forming metallic liquid, Sci. Rep. **5**, 10956 (2015).
[72] M. Li, Z. Yue, Y. Chen, H. Tong, H. Tanaka, and P. Tan, Revealing thermally-activated nucleation pathways of diffusionless solid-to-solid transition, Nat. Commun. **12**, 4042 (2021).
[73] Z. D. Jastrzebski, *Nature and Properties of Engineering Materials* (John Wiley and Sons, New York, 1959).
[74] L. Wang and J. J. Hoyt, Layering misalignment and negative temperature dependence of interfacial free energy of B2-liquid interfaces in a glass forming system, Acta Mater. **219**, 117259 (2021).
[75] H.-K. Mao, X.-J. Chen, Y. Ding, B. Li, and L. Wang, Solids, liquids, and gases under high pressure, Rev. Mod. Phys. **90**, 015007 (2018).
[76] S. Singh, M. G. Gorman, P. G. Heighway, J. V. Bernier, D. McGonegle, H. J. Lee, B. Nagler, J. H. Eggert, and R. F. Smith, Unexpected observation of disorder and multiple phase-transition pathways in shock-compressed Zr, Phys. Rev. Lett. **133**, 096101 (2024).
[77] J. Park, J.-Y. Hwang, K. H. Lee, S.-G. Kim, K. Lee, and S. W. Kim, Tuning the spin-alignment of interstitial electrons in two-dimensional Y_2C electride via chemical pressure, J. Am. Chem. Soc. **139**, 17277 (2017).
[78] K. Lee, S. W. Kim, Y. Toda, S. Matsuishi, and H. Hosono, Dicalcium nitride as a two-dimensional electride with an anionic electron layer, Nature (London) **494**, 336 (2013).
[79] S. Y. Lee *et al.*, Ferromagnetic quasi-atomic electrons in two-dimensional electride, Nat. Commun. **11**, 1526 (2020).
[80] S. Y. Lee, D. C. Lim, M. S. Khan, J. Y. Hwang, H. S. Kim, K. H. Lee, and S. W. Kim, Magnetic quasi-atomic electrons driven reversible structural and magnetic transitions between electride and its hydrides, Nat. Commun. **14**, 5469 (2023).
[81] S. Kim *et al.*, Quantum electron liquid and its possible phase transition, Nat. Mater. **21**, 1269 (2022).
[82] L. Zhao, GitHub (2025), https://github.com/LongZhao1993/DataQuasi-atom-PRL2025.

Supplemental Material for **"Fast crystallization driven by quasiatomic electrons at ultralow temperatures"**

Long Zhao[1], Hongxiang Zong[1*], Artem R. Oganov[2], Xiangdong Ding[1*], Jun Sun[1] & Graeme J. Ackland[3]

[1]State Key Laboratory for Mechanical Behavior of Materials, Xi'an Jiaotong University, Xi'an 710049, China

[2]Skolkovo Institute of Science and Technology, Skolkovo Innovation Center, Bolshoy Boulevard 30, bldg. 1, Moscow, 121205, Russia

[3]Centre for Science at Extreme Conditions (CSEC), School of Physics and Astronomy, University of Edinburgh, Edinburgh EH9 3FD, UK

*To whom correspondence should be addressed. E-mail: zonghust@mail.xjtu.edu.cn and dingxd@mail.xjtu.edu.cn.

Note 1: Temperature-dependent machine learning potential (TD-MLP)

Dense electride liquids exhibit unique electronic characteristics that distinguish them from conventional atomic and molecular liquids [1-3]. Here, we use the electron entropy as a critical indicator for describing such intrinsic electronic structures. Therefore, a TD-MLP was developed for dense potassium, which explicitly incorporates the contribution of electron-smearing effects into the total energy calculation. In this framework, two types of local atomic descriptors are designed: 1) descriptors that solely rely on the local atom arrangement, a common approach utilized in machine learning potential [4,5]; 2) descriptors that, in addition to the local atomic structures, also account for the electron and ion temperatures, which are designed to capture the temperature-dependent of both entropy and enthalpy based on Sommerfeld model [6]. These descriptors are mapped into the corresponding atomic energies/forces with the simple kernel ridge regression method.

The TD-MLP is directly learned from a high-fidelity reference database of first-principle calculations using the Vienna Ab initio Simulation Package (VASP) code [7]. More importantly, the electronic entropy is considered in all ab initio molecular dynamics simulations (AIMD) with the temperature-adjusted Fermi-Dirac smearing method [8]. To describe the crystallization kinetics of dense electride liquid, more than 46180 configurations were accumulated from the molecular dynamics simulations for different structures, including face-centered cubic (FCC), body-centered cubic (BCC) and their liquid structures as well as structure derived from crystallization processes of their supercooled liquids at a wide range of temperatures and pressures from 50 – 900

K and 12 – 18 GPa. The details of sample strategies of these configurations can be found in section 1.2. In this way, the TD-MLP autonomously navigates towards uncharted areas of the configuration space that require further exploration. The training and testing datasets are randomly collected from the reference dataset with a proportion of 9:1. The detailed formalism of these descriptors and benchmarks about the TD-MLP can be found in section 1.1. More importantly, to verify the role of electronic entropy in the dynamics of the dense electride state, we trained two additional MLPs: one without explicit electronic contributions to the total energy (referred to as MLP-1) and another using only the potential energy (referred to as MLP-2). Notably, all MLPs, including TD-MLP, MLP-1, and MLP-2, were trained on the same set of configurations.

1.1 Formulation of atomic descriptors

Inspired by Ackland's seminal research [6], the TD-MLP contains two categories of atomic descriptors. One is a structure descriptor, which is encoded by solely atomic position; Another one is a temperature-dependent structure descriptor, which is encoded by both atomic position and temperatures of electrons and ions. The formulation of both descriptors is delineated as follows:

1.1.1 Structure descriptor

The structure descriptors include pairwise interactions, 6 three-body interactions, and 2 many-body terms. Each descriptor contributes an amount to the total energy via a kernel with the proportionality constants, ω, which are machine-learned.

The pairwise descriptors are built using Gaussians with a smooth cutoff in the form:

$$V_i^{pair,s} = \sum_{j \neq i} \exp -(r_{ij} / \eta_s)^2 f_c(r_{ij}) \quad (1)$$

Where r_{ij} is the distance between atoms i and j, η_s is the Gaussian function width; $f_c(r_{ij})$ = 0.5 (1.0 + cos ($\pi r_{ij}/R_c$)) is a smooth function inside a cutoff distance R_c, and is zero elsewhere. We use eight values of η_s: 1.00, 1.346, 1.811, 2.432, 3.281, 4.416, 5.944, 8.00.

There are 6 three-body descriptors defined as

$$V_i^{3b,s} = \sum_{k>j \neq i} g_s(\cos\theta_{jik}) \exp)((-r_{ij}^2 - r_{ik}^2) / \eta_s^2) f_c(r_{ij}) f_c(r_{ik}) \quad (2)$$

Where θ_{jik} is the angle between atoms i, j, and k centered on atom i. $g_s(\theta_{jik})$ is one of several polynomial functions of the angle.

Finally, there are 2 many-body descriptors based on a local density in the spirit of the embedded atom method:

$$\rho_i^s = \sum_{j \neq i} \exp(-(r_{ij} - u)^2 / \sigma^2) f_c(r_{ij}) \quad (3)$$

The parameters u and σ were adjustable parameters for many-body descriptors. Specifically, the parameter u is determined from structural information, such as the first few neighbor atomic distances. The parameter σ is related to the s, p, or d-band electronic structure [9]. The many-body term is constructed as :

$$V_i^{MB,s}(\rho_i) = \rho_i \ln(\rho_i) \quad (4)$$

1.1.2 Temperature-dependent structure descriptor

According to Sommerfeld‘s theory [10], the temperature-dependent contribution to the electronic free energy depends on temperature and the density of states at the Fermi energy as

$$F_{sommerfeld}(T) \propto T^2 n(E_F) \quad (5)$$

To include Sommerfeld effects in molecular dynamics, we need to design the descriptors to explicitly account for the temperature-dependent contribution to electronic free energy. This approach enables our machine-learning potential to accurately capture the electronic entropy effect. Considering the efficiencies and accuracy, our temperature-dependent structure descriptors include one pairwise interaction and one three-body interaction. More importantly, both pairwise and three-body interactions are divided into electron and ion temperature parts. The electron temperatures correspond to the Fermi-Dirac smearing setting, while the ion temperatures are extracted from AIMD simulation results.

The pairwise term involving electron temperatures is defined as

$$V_i^{pair,T_{ele}} = f(T_{ele}) \sum_{j \neq i} \exp((r_{ij} - u)^2 / \eta_s) H(r_o + d - r_{ij}) H(r_{ij} - r_o) f_c(r_{ij}) \quad (6)$$

The pairwise term involving ion temperatures is defined as

$$V_i^{pair,T_{ion}} = f(T_{ion}) \sum_{j \neq i} \exp((r_{ij} - u)^2 / \eta_s) H(r_o + d - r_{ij}) H(r_{ij} - r_o) f_c(r_{ij}) \quad (7)$$

Where the $f(T)$ is one of the polynomial functions of electron and ion temperature; u, r_o, and d are adjusted parameters, and determined by atomic and band structures of dense potassium.

The three-body term involving electron temperatures is defined as:

$$V_i^{3b,T_{ele}} = f_T(T_{ele}) \sum_{j \neq i} g_T(\cos\theta_{jik}) \exp(((r_{ij} - u)^2 (r_{ik} - u)^2 / \eta_s^2)) f_c(r_{ij}) f_c(r_{ik}) \quad (8)$$

The three-body term involving ion temperatures is defined as:

$$V_i^{3b,T_{ion}} = f_T(T_{ion}) \sum_{j \neq i} g_T(\cos\theta_{jik}) \exp(((r_{ij} - u)^2 (r_{ik} - u)^2 / \eta_s^2)) f_c(r_{ij}) f_c(r_{ik}) \quad (9)$$

The structure and temperature-dependent structure descriptors are initially normalized to [0,1] before the regression learning. Here, we used the kernel ridge

regression (KRR) method, capable of handling both linear and nonlinear relationships. The local energy E_i^{tot} is given by a linear combination of descriptors and weights:

$$E_i^{tot} = \sum_t w_t V_t^{s,T} + b_0 \quad (10)$$

The machine-learned coefficients w_t and b_0 are generated by the kernel ridge regression method [11].

The in-house TD-MLP was implemented as a plug into the LAMMPS code [12].

1.2 Sampling strategies for the reference dataset

To accumulate the reference dataset for training the TD-MLP of potassium (K), we utilize two types of sampling strategies:

1.2.1 AIMD trajectory sampling

This aims to capture the initial phase space of electride potassium, enabling subsequent MD iteration sampling. To ensure a comprehensive collection of diverse atomic environments, we considered possible structures of K, including FCC, BCC, their different defective structures (e.g., vacancies, interstitial atoms, dislocations, and grain boundaries), corresponding liquid and supercooled liquid structures. These structures were subjected to AIMD simulations at a wide range of pressures (12 – 18 GPa) and temperatures (50 K – 900 K). Each simulation was run for approximately 30.0 ps, and structures were sampled from the trajectories at 0.03 ps intervals.

1.2.2 Sampling from classical MD iterations

Based on the initial AIMD-derived dataset, we constructed a preliminary TD-MLP. We then performed long-timescale (~ 1.0 ns) classical MD simulations for a variety of

structures, particularly liquids at different degrees of supercooling. This approach overcomes the timescale limitations of AIMD, enabling a more comprehensive exploration of nonequilibrium structures during the crystallization of potassium under various pressures. Independent configurations were selected from each trajectory based on time intervals exceeding the correlation time (~ 5.0 ps). These configurations underwent static DFT calculations with Fermi-Dirac smearing, and their results were integrated into the dataset to enhance the performance and transferability of the TD-MLP. This iterative strategy has been successfully applied to constructing MLPs for both molecular hydrogen [13] and potassium [14] at high pressures.

1.3 Benchmarks

To evaluate the accuracy of the TD-MLP model, we first calculated the mean absolute error (MAE) for both atomic energies and forces, and compared these results with the corresponding density functional theory (DFT) calculations, as shown in Figs. S1(a)-(b). The low MAE for potential energy (2.7 meV/atom) and atomic forces (8.2 meV/Å·atom) demonstrates the high fidelity of our TD-MLP compared to DFT. The broad distribution of energies and forces suggests that the configuration space on the potential energy surface is sufficiently sampled. We also computed the MAE for a version of the MLP that excludes electron entropy contributions, while maintaining the same number of descriptors as the TD-MLP. The corresponding results, as shown in Figs. S1(c)-(d), reveals a significant deterioration in accuracy compared to the TD-MLP: atomic energies (MAE = 5.2 meV/atom) and forces (MAE = 17.0 meV/Å·atom) are

notably less accurate. This discrepancy underscores the critical role of electron entropy, highlighting the necessity of explicitly incorporating electronic entropy into the MLP for accurate predictions of crystallization kinetics in supercooled electride liquids.

In addition, we compared the temperature dependence of pressure for FCC potassium at three fixed volumes between the TD-MLP and AIMD results, as shown in Fig. S2. The results show excellent agreement between the two methods. Furthermore, the radial distribution functions (RDFs) of liquid and supercooled liquid potassium at 15 GPa from both TD-MLP and DFT calculations exhibit remarkable overlap, as shown in Fig. S3. These findings demonstrate that the TD-MLP accurately captures the structural features and temperature-dependent thermodynamic properties of electride states.

Note 2: Ab initio molecular dynamics (AIMD) simulation

AIMD simulations are carried out by using the Vienna ab initio simulation (VASP) code [7]. The projector augmented wave potentials (PAW) and the Perdew–Burke–Ernzerhof (PBE) Exchange-correlation functional [15] were employed in the calculations. Previous studies [16,17] have demonstrated that including the filled (n-1) sp electron shell immediately below the outer n s valence electron in the valence space is necessary to correctly describe the alkali metals at high pressures where these inner core electron wavefunctions begin to overlap. Therefore, the K pseudopotential with the configuration $3s^2 3p^6 4s^1$ is employed in all VASP calculations, as it has been shown to accurately reproduce the pressure-induced phase transition sequence and the

corresponding transition pressures observed in experiments [14,17-19]. The energy cutoff is set as 450.0 eV. The optimization of FCC and BCC at 0 K and different pressures was achieved using a primitive cell with a grid density of 0.02 $Å^{-1}$ for *k*-point sampling in the Brillouin zone. AIMD simulations ran at a fixed density (NVT) with a Nosé–Hoover thermostat using a timestep of 1.0 fs, temperature-adjusted Fermi-Dirac smearing [8], and sampling of up to 18.0 ps. Atomic forces are calculated using the Hellmann-Feynman theorem. In different isothermal simulations, the ions in different supercells range from 54 to 108 of BCC, FCC, their liquids, and supercooled liquids with different supercooling temperatures. Our AIMD simulations [Fig. S4], together with previous results [20-22], confirm that such supercell sizes can reliably capture the quasi-atomic electronic behavior in electride systems. The AIMD is not large enough to describe the crystallization process, which is why the TD-MLP is needed.

Note 3: TD-MLP enhanced molecular dynamics simulation

Classical molecular dynamics (CMD) simulations were performed using the LAMMPS package [12]. To investigate the crystal growth rate of different surfaces of potassium's supercooled electride liquids, we created the crystal-liquid interface models. The initial simulation box contains 6×6 transformed unit cells in the *x*-*y* plane and ~ 20 transformed unit cells along the *z* direction, with a total of ~ 11,000 atoms [see Fig. S5]. Then crystal particles of 4 unit cells in the upper were pinned, and the rest of the crystals were melted into liquids at a temperature (T = 900 K) above melting points of potassium at 15 GPa. The melting temperature (T_m) at this pressure, determined using the two-phase coexistence method [23,24], is 515 ± 10 K [Fig. S6], in good agreement with the

experimental result [18]. Each simulation was carried out using a timestep of 1.0 fs, and periodic boundary conditions were applied along all three dimensions. The Nosé–Hoover thermostat [25] and Parrinello–Rahman barostat [26] were used for controlling the temperature and pressure, respectively. The crystal/liquid interface was detected by identifying the crystal front using polyhedral template matching, as implemented in the Ovito package [27]. This method ensures reliable structural identification, even in the presence of strong thermal fluctuations and strain. Additionally, to investigate the nucleation behavior, a bulk electride liquid was prepared by melting a face-centered cubic (FCC) structure containing 2304 or 4608 atoms at temperatures above the melting point (T_m), under isothermal–isobaric (NPT) conditions at a specified pressure. Subsequently, the system was rapidly quenched to the target temperature for isothermal annealing, allowing for crystallization to proceed. The crystallization process was monitored using bond-orientational order parameters, which were employed to identify crystalline particles within the supercooled liquid. A detailed description of the definition and calculation of these parameters is available in previous studies [28,29]. To ensure statistical reliability, ten independent simulations were conducted to obtain ensemble averages.

Note 4: Thermodynamic driving force

In our simulations, the thermodynamic driving force for crystallization Δu is estimated empirically as:

$$\Delta\mu = \Delta H_m \left(\frac{T_m - T}{T_m}\right) \tag{11}$$

Where ΔH_m is the enthalpy of fusion per atom at the melting temperature T_m. To measure ΔH_m (T_m), we created an equilibrium solid and liquid at T_m, respectively, and calculated the enthalpy difference directly. The T_m of potassium at 15 GPa is determined using solid-liquid coexistence models. Additionally, we employed the capillary fluctuation method (CFM) to calculate the interfacial stiffness of the electride state. This method has been extensively used to study the solid-liquid interfacial stiffness of various systems, including metals with different crystal phases and alloys [30,31]. A detailed description of this method can be found in Ref. [32]. To minimize computational costs and reduce measurement errors, the simulated model was designed to be quasi-two-dimensional, with the length of the interfaces (~15 nm) significantly larger than their width (1.5 nm). Three independent simulations were performed to obtain ensemble averages.

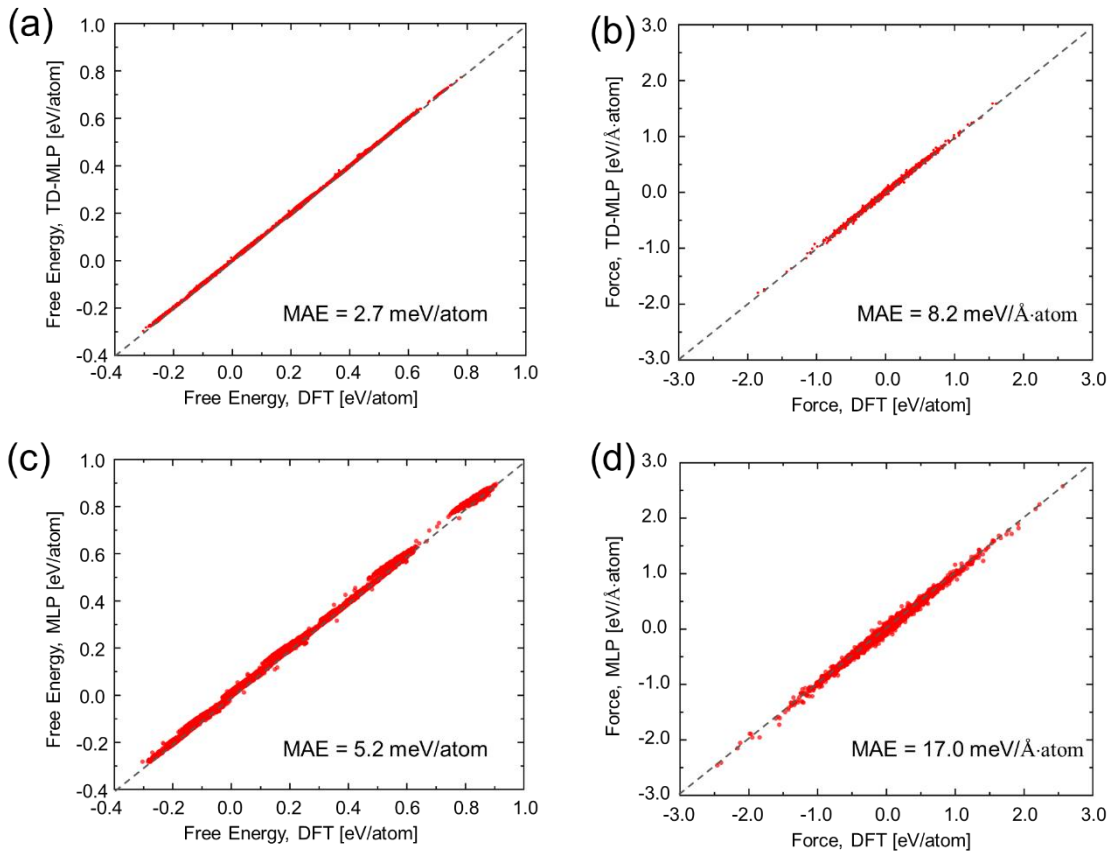

FIG. S1. (a)-(b) Comparisons of energies and atomic forces between DFT and the TD-MLP model. (c)-(d) denote the results between DFT and MLP model without electronic entropy contribution. The black dashed lines are guides for perfect matches.

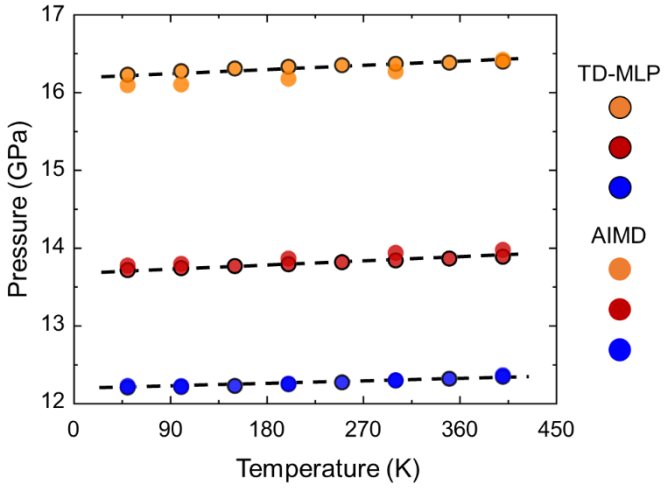

FIG. S2. Comparisons of temperature-dependent pressure of FCC potassium at three fixed volumes between AIMD results and TD-MLP model. The excellent agreement between them indicates the high quality of TD-MLP.

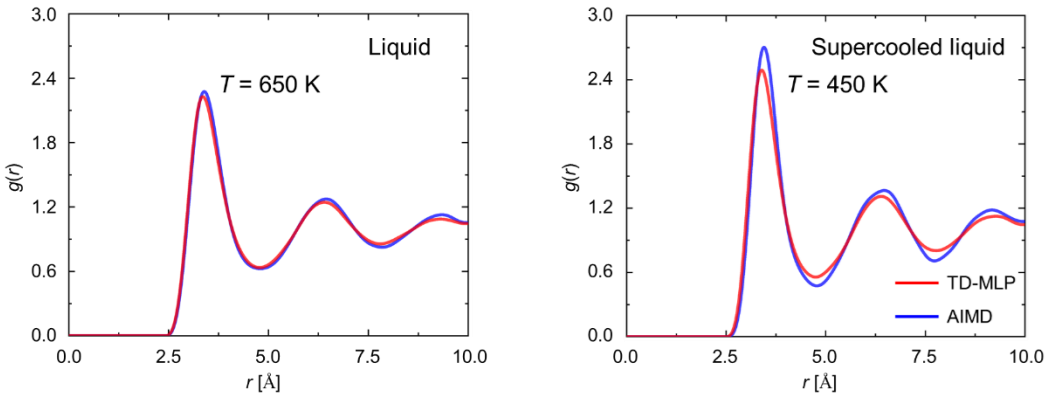

FIG. S3. Comparisons of radial distribution functions of liquid and supercooled liquid at 15 GPa between AIMD results and TD-MLP model. The reasonable agreement between them indicates a good performance of TD-MLP.

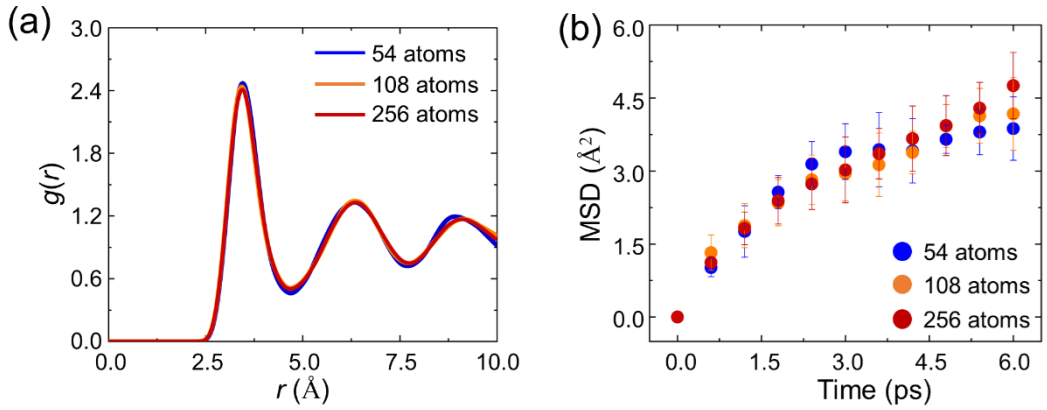

FIG. S4. Structural and dynamic properties of supercooled electride liquids with different system sizes of 54, 108, and 256 atoms, obtained from AIMD simulations at 15 GPa and 400 K. (a)-(b) Radial distribution functions (RDFs) and time evolution of mean square displacements (MSDs), respectively, for the three systems.

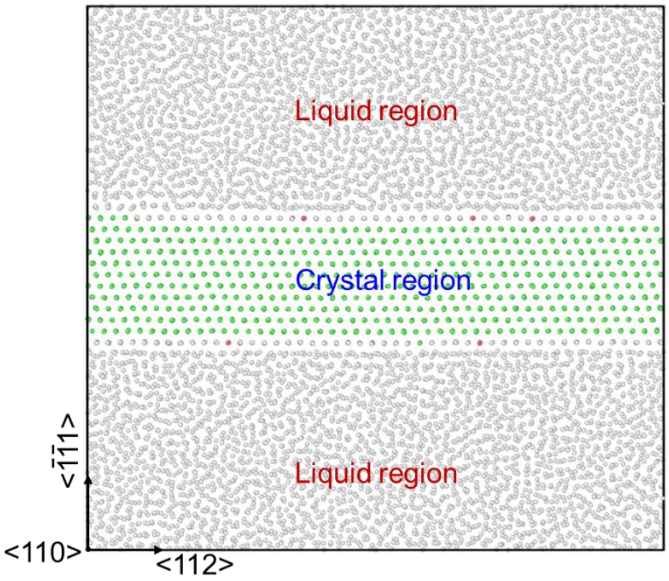

FIG. S5. Schematic illustration of prototypical $(111)_{FCC}$ solid-liquid interfacial model for electride potassium at 15 GPa. Green spheres represent atoms in the FCC crystalline structure, while white spheres denote atoms in the liquid phases.

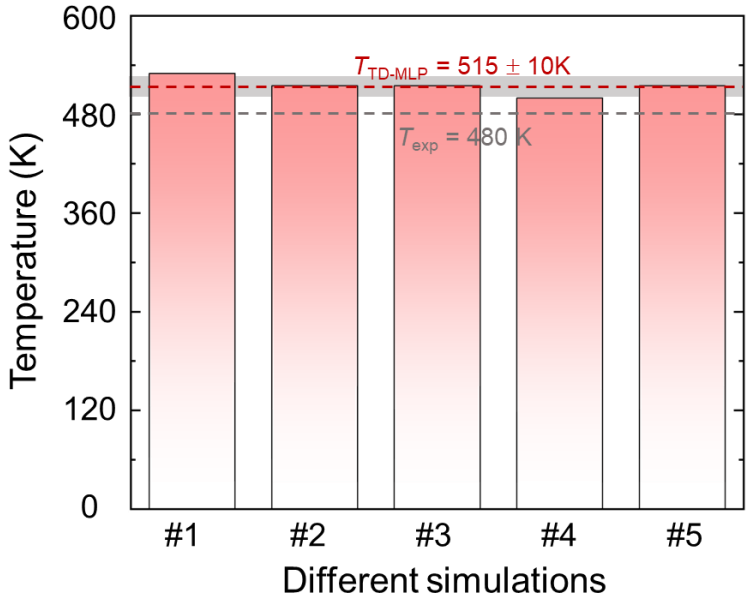

FIG. S6. Predicted melting point of potassium at 15 GPa by TD-MLP. Five independent simulations were performed using a solid-liquid two-phase model consisting of 9216 atoms, each with a different initial random seed. The predicted melting point (red dashed line) is 515 ± 10 K, in good agreement with the experimental value (grey dashed line, T_m = 480 K) [18].

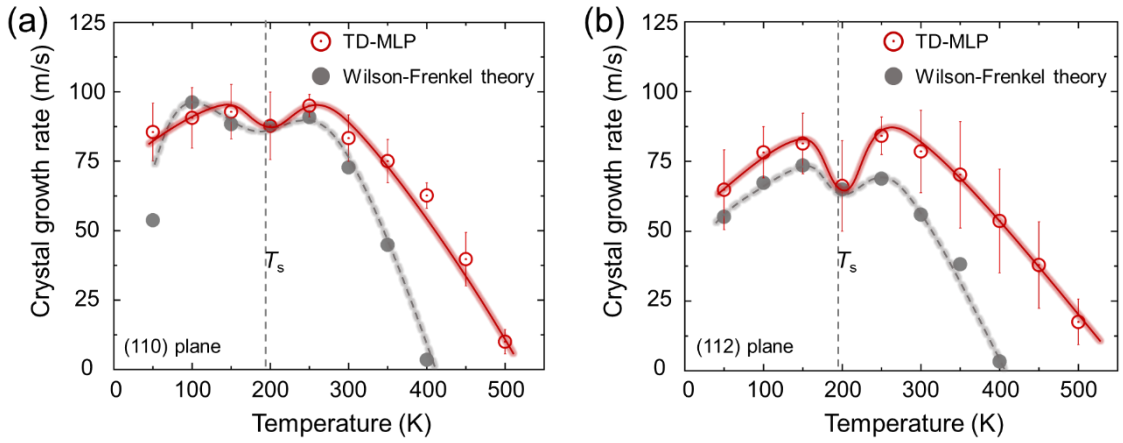

FIG. S7. Crystal growth rate in dense electride liquid along different crystal/liquid surfaces. Temperature dependence of the average crystal growth rate for (a) $(110)_{FCC}$ and (b) $(112)_{FCC}$ planes, respectively. Red circles represent results from the TD-MLP model, showing a double *C*-curve phenomenon separated by a characteristic temperature (T_s = 200 K). Grey circles correspond to crystal growth rates predicted by the modified Wilson-Frenkel theory [28]. Solid and dashed lines are guides to the eye.

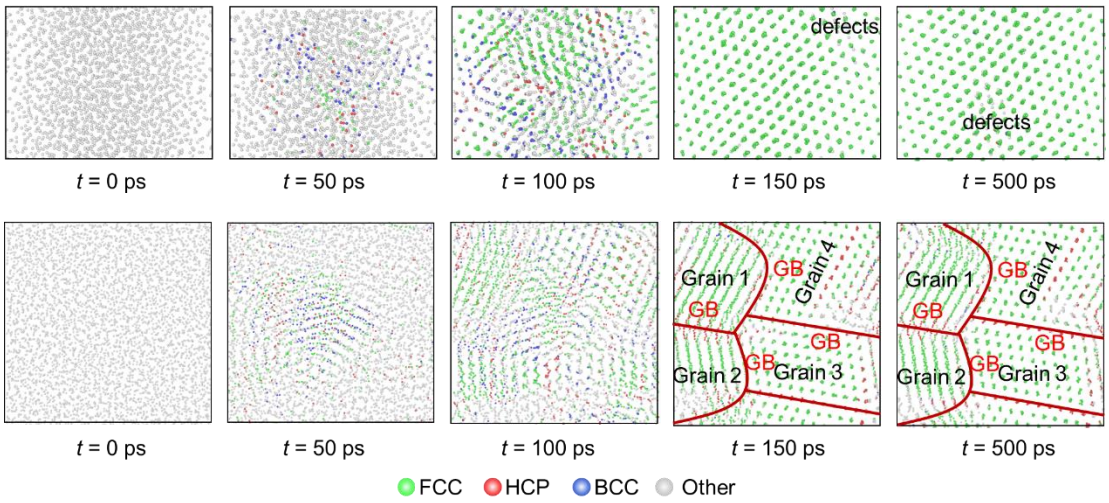

FIG. S8. Structural evolution of a supercooled electride liquid containing 2304 and 4,608 atoms at 15 GPa and 150 K. The smaller sample crystallizes into a single-crystal structure with a few defects (upper plane), while the larger sample solidifies into a polycrystalline structure characterized by grain boundaries (GBs) and grains with different crystal orientations (lower panel). The atoms are colored by the polyhedral template matching method: green: FCC, blue: BCC, red: HCP, and white: others.

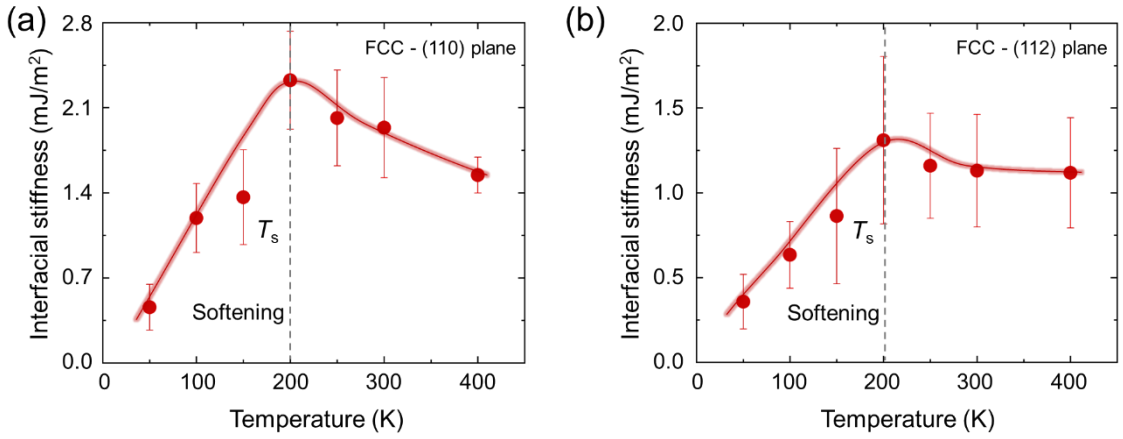

FIG. S9. Temperature dependence of interfacial stiffness along (a) $(110)_{FCC}$ and (b) $(112)_{FCC}$ crystal/liquid surfaces, respectively. The dashed line indicates the crossover temperature of the thermodynamic properties. Solid lines are guides to the eye.

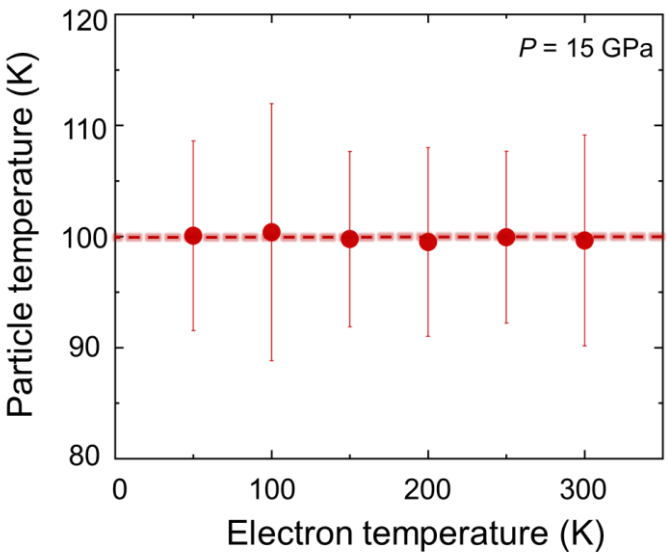

FIG. S10. Average particle temperature of deeply supercooled electride liquid (T_p =100 K) at different electron temperatures. The results show that the particle temperature is independent of the electron temperature upon AIMD simulations. The particle temperature is averaged over approximately 5.0 ps of trajectories after thermal equilibrium.

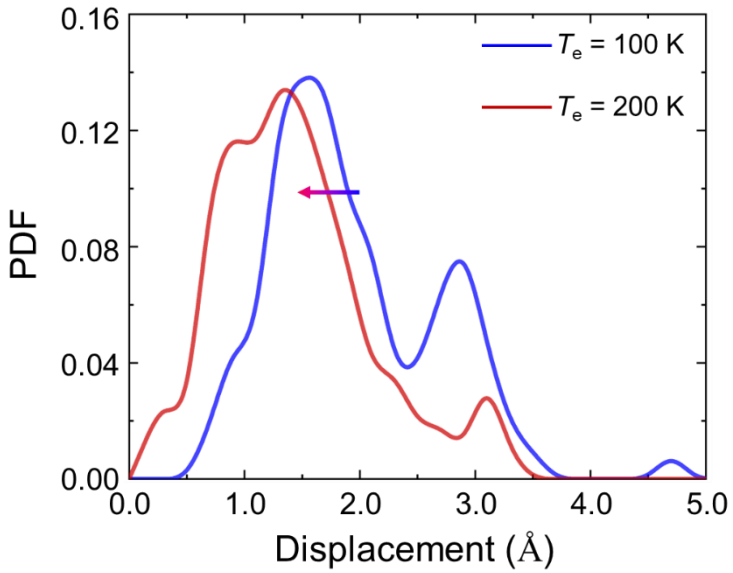

FIG. S11. The probability distribution functions (PDF) of atomic displacements within 5.0 ps at T_e = 100 K and 200 K. The results demonstrate a significant reduction in atomic displacement with an increase in electronic temperature.

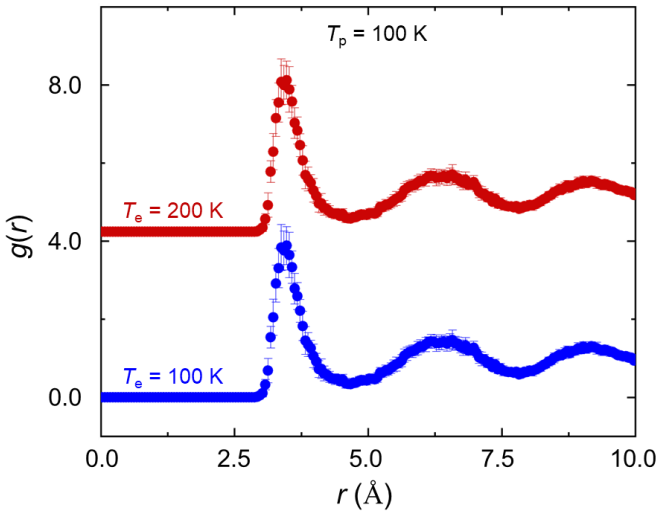

FIG. S12. Comparison of radial distribution functions (RDFs) for liquids at varying electronic temperatures (T_e) and constant particle temperature (T_p). The RDFs for liquids at $T_e = 200$ K and $T_e = 100$ K are represented by red and blue circles, respectively. All RDFs were computed by averaging over 30 independent snapshots extracted from AIMD isothermal trajectories (108 atoms), following an equilibration period of 2.0 ps.

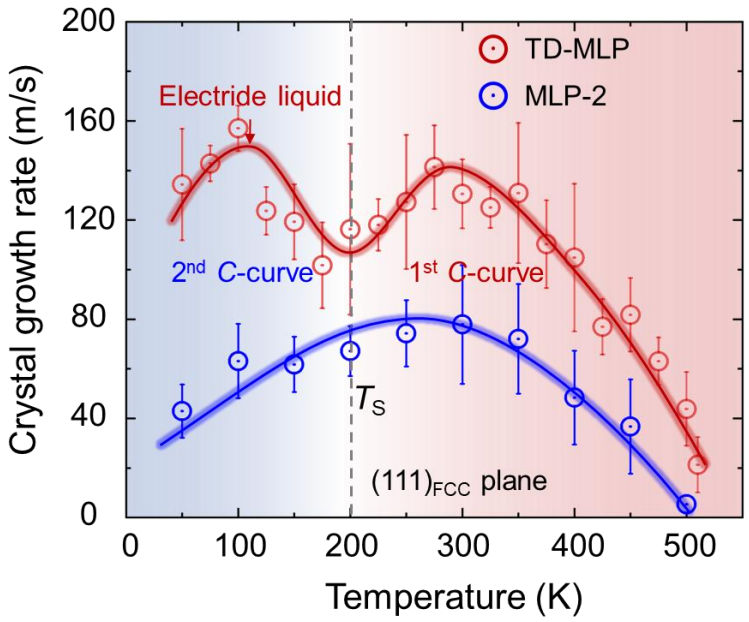

FIG. S13. Temperature dependence of the average crystal growth rate for (111)FCC plane. Red circles represent results from the TD-MLP model, showing a double *C*-curve phenomenon separated by a characteristic temperature (T_s = 200 K). In contrast, predictions from an alternative MLP-2 model, trained exclusively on potential energy, exhibit a single *C*-curve (blue circles). Each data point is averaged over ten independent simulations, with error bars denoting the standard deviation. Solid and dashed lines are guides to the eye.

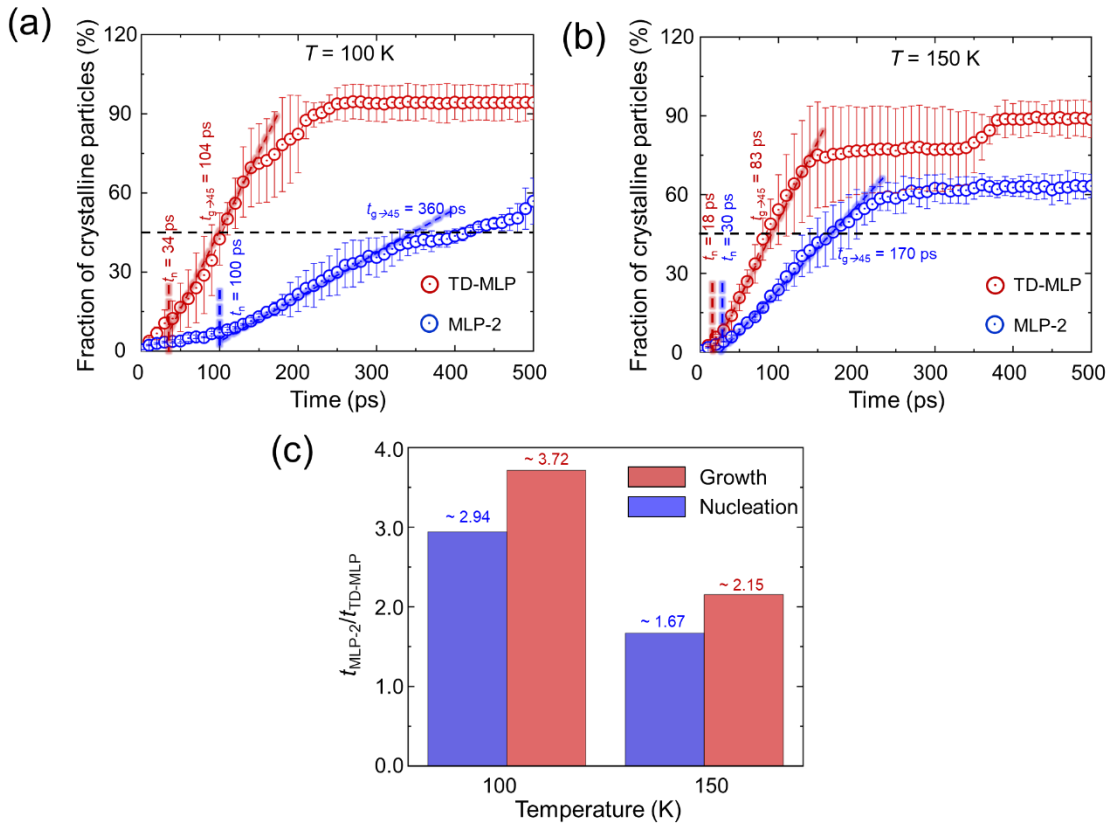

FIG. S14. Comparison of crystallization dynamics of supercooled liquid using TD-MLP and MLP-2. (a)-(b) Time evolution of the fraction of crystalline particles for supercooled liquid at 100 K and 150 K, respectively. The t_n and $t_{g\to45}$ denote the nucleation time and the time required to reach 45% of the fraction of crystalline particles, respectively. These values are obtained based on the Kolmogorov–Johnson–Mehl–Avrami (KJMA) model [33]. (c) Acceleration factors for both nucleation and growth stages at 100 K and 150 K are calculated as the ratio of the nucleation and growth durations from MLP-2 and TD-MLP.

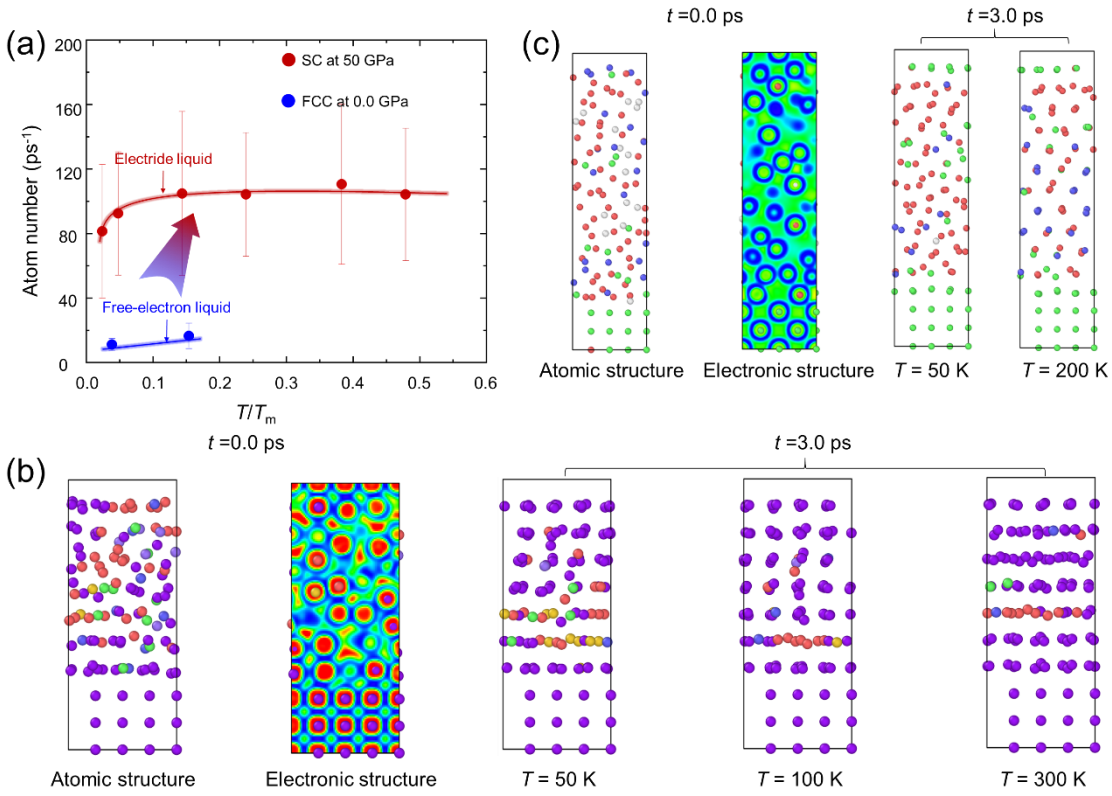

FIG. S15. Crystallization kinetics of supercooled liquid with different electronic states for calcium. (a) Average crystal growth rate of supercooled liquid for Ca at $(100)_{FCC}$ and $(100)_{SC}$ crystal-liquid surface at 0 GPa and 50 GPa. The SC and FCC represent the simple cubic and face-centered cubic structures of Ca. The temperature is normalized by their melting points (T_m_FCC = 1300 K and T_m_SC = 2089 K) at corresponding pressures. Under ambient conditions, calcium adopts an FCC structure, exhibiting a nearly free-electron behavior [21]. At 50 GPa, calcium transitions into an SC structure with distinct electride characteristics [21]. Notably, the growth rate of the supercooled electride liquid is significantly higher and remains nearly constant over a broad temperature range, extending to ultralow temperatures (~0.1 T_m). This contrasts with the temperature-dependent crystallization observed in the free-electron liquid, underscoring the ultrafast crystallization kinetics of the deeply supercooled electride

liquids and reinforcing our conclusions. (b)-(c) Electronic structure and crystallization processes at varying temperatures for the $(100)_{FCC}$ and $(100)_{SC}$ crystal-liquid interfaces. As expected, the SC liquid shows electride characteristics, whereas the FCC counterpart exhibits nearly free-electron behavior. The local structures are identified using polyhedral template matching, implemented via the Ovito package [27].

[1] X. Dong and A. R. Oganov, in Correlations in Condensed Matter Under Extreme Conditions: A Tribute to Renato Pucci on the Occasion of his 70th Birthday, edited by G. G. N. Angilella, and A. La Magna (Springer International Publishing, Cham, 2017).

[2] S. Racioppi and E. Zurek, High-Pressure Electrides: A Quantum Chemical Perspective, Annu. Rev. Mater. Res. **55**, 1 (2025).

[3] H. Hosono and M. Kitano, Advances in Materials and Applications of Inorganic Electrides, Chem. Rev. **121**, 3121 (2021).

[4] A. P. Bartók, M. C. Payne, R. Kondor, and G. Csányi, Gaussian Approximation Potentials: The Accuracy of Quantum Mechanics, without the Electrons, Phys. Rev. Lett. **104**, 136403 (2010).

[5] H. Wang, L. Zhang, J. Han, and W. E, DeePMD-kit: A deep learning package for many-body potential energy representation and molecular dynamics, Comput. Phys. Commun. **228**, 178 (2018).

[6] G. J. Ackland, Temperature dependence in interatomic potentials and an improved potential for Ti, J. Phys. Conf. Ser. **402**, 012001 (2012).

[7] G. Kresse and J. Furthmüller, Efficient iterative schemes for ab initio total-energy calculations using a plane-wave basis set, Phys. Rev. B **54**, 11169 (1996).

[8] N. D. Mermin, Thermal Properties of the Inhomogeneous Electron Gas, Phys. Rev. **137**, A1441 (1965).

[9] G. J. Ackland and S. K. Reed, Two-band second moment model and an interatomic potential for caesium, Phys. Rev. B **67**, 174108 (2003).

[10] L. Zhao, H. Zong, X. Ding, J. Sun, and G. J. Ackland, Commensurate-incommensurate phase transition of dense potassium simulated by machine-learned interatomic potential, Phys. Rev. B **100**, 220101 (2019).

[11] H. Li, L. Zhao, X. Ding, H. Zong, T. Lookman, and J. Sun, Mechanism of the β to ω phase transformation in shock compressed Zr-Nb alloys, Phys. Rev. B **110**, 134105 (2024).

[12] S. Plimpton, Fast Parallel Algorithms for Short-Range Molecular Dynamics, J. Comput. Phys. **117**, 1 (1995).

[13] H. Zong, H. Wiebe, and G. J. Ackland, Understanding high pressure molecular hydrogen with a hierarchical machine-learned potential, Nat. Commun. **11**, 5014 (2020).

[14] H. Zong, V. N. Robinson, A. Hermann, L. Zhao, S. Scandolo, X. Ding, and G. J. Ackland, Free electron to electride transition in dense liquid potassium, Nat. Phys. **17**, 955 (2021).

[15] Y. Wang and J. P. Perdew, Correlation hole of the spin-polarized electron gas, with exact small-wave-vector and high-density scaling, Phys. Rev. B **44**, 13298 (1991).

[16] C. J. Pickard and R. J. Needs, Ab initio random structure searching, Journal of Physics: Condensed Matter **23**, 053201 (2011).

[17] G. Woolman, V. Naden Robinson, M. Marqués, I. Loa, G. J. Ackland, and A. Hermann, Structural and electronic properties of the alkali metal incommensurate phases, Phys. Rev. Mater. **2**, 053604 (2018).

[18] E. E. McBride, K. A. Munro, G. W. Stinton, R. J. Husband, R. Briggs, H. P. Liermann, and M. I. McMahon, One-dimensional chain melting in incommensurate potassium, Phys. Rev. B **91**, 144111 (2015).

[19] D. N. Polsin *et al.*, Structural complexity in ramp-compressed sodium to 480 GPa, Nat. Commun. **13**, 2534 (2022).

[20] S. Ayrinhac, V. N. Robinson, F. Decremps, M. Gauthier, D. Antonangeli, S. Scandolo, and M. Morand, High-pressure transformations in liquid rubidium, Phys. Rev. Mater. **4**, 113611 (2020).

[21] Y. Wang, J. Wang, A. Hermann, C. Liu, H. Gao, E. Tosatti, H.-T. Wang, D. Xing,

and J. Sun, Electronically driven 1D cooperative diffusion in a simple cubic crystal, Phys. Rev. X **11**, 011006 (2021).

[22] E. Oren, D. Kartoon, and G. Makov, Machine learning-based modeling of high-pressure phase diagrams: Anomalous melting of Rb, J. Chem. Phys. **157**, 014502 (2022).

[23] D. Alfè, M. J. Gillan, and G. D. Price, Complementary approaches to the ab initio calculation of melting properties, J. Chem. Phys. **116**, 6170 (2002).

[24] D. Alfè, Melting curve of MgO from first-principles simulations, Phys. Rev. Lett. **94**, 235701 (2005).

[25] S. Nosé, A unified formulation of the constant temperature molecular dynamics methods, J. Chem. Phys. **81**, 511 (1984).

[26] M. Parrinello and A. Rahman, Polymorphic transitions in single crystals: A new molecular dynamics method, J. Appl. Phys. **52**, 7182 (1981).

[27] A. Stukowski, Visualization and analysis of atomistic simulation data with OVITO–the open visualization tool, Model. Simul. Mater. Sci. Eng. **18**, 015012 (2010).

[28] Y.-C. Hu and H. Tanaka, Revealing the role of liquid preordering in crystallisation of supercooled liquids, Nat. Commun. **13**, 4519 (2022).

[29] P. Tan, N. Xu, and L. Xu, Visualizing kinetic pathways of homogeneous nucleation in colloidal crystallization, Nat. Phys. **10**, 73 (2014).

[30] Y. Yin, Y. Zhu, S. Liu, D. Zheng, and M. Yi, Far-from-equilibrium solid–liquid interfacial properties of aluminum, Acta Mater. **278**, 120279 (2024).

[31] C. Qi, J. F. Li, B. Xu, L. T. Kong, and S. Zhao, Atomistic characterization of solid-liquid interfaces in the Cu-Ni binary alloy system, Comput. Mater. Sci. **125**, 72 (2016).

[32] J. Hoyt, M. Asta, and A. Karma, Method for computing the anisotropy of the solid-liquid interfacial free energy, Phys. Rev. Lett. **86**, 5530 (2001).

[33] V. Erukhimovitch and J. Baram, Nucleation and growth transformation kinetics, Phys. Rev. B **51**, 6221 (1995).